PHYSICAL REVIEW E **70**, 031905 (2004)

Self-organized pattern formation in motor-microtubule mixtures

Sumithra Sankararaman* and Gautam I. Menon†
The Institute of Mathematical Sciences, CIT Campus, Taramani, Chennai 600 113, India

P. B. Sunil Kumar‡
Department of Physics, Indian Institute of Technology Madras, Chennai 600 036, India

(Received 24 November 2003; revised manuscript received 5 April 2004; published 16 September 2004)

We model the stable self-organized patterns obtained in the nonequilibrium steady states of mixtures of molecular motors and microtubules. In experiments [Nédélec *et al.*, Nature (London) **389**, 305 (1997); Surrey *et al.*, Science **292**, 1167 (2001)] performed in a quasi-two-dimensional geometry, microtubules are oriented by complexes of motor proteins. This interaction yields a variety of patterns, including arrangements of asters, vortices, and disordered configurations. We model this system via a two-dimensional vector field describing the local coarse-grained microtubule orientation and two scalar density fields associated to molecular motors. These scalar fields describe motors which either attach to and move along microtubules or diffuse freely within the solvent. Transitions between single aster, spiral, and vortex states are obtained as a consequence of confinement, as parameters in our model are varied. For systems in which the effects of confinement can be neglected, we present a map of nonequilibrium steady states, which includes arrangements of asters and vortices separately as well as aster-vortex mixtures and fully disordered states. We calculate the steady state distribution of bound and free motors in aster and vortex configurations of microtubules and compare these to our simulation results, providing qualitative arguments for the stability of different patterns in various regimes of parameter space. We study the role of crowding or "saturation" effects on the density profiles of motors in asters, discussing the role of such effects in stabilizing single asters. We also comment on the implications of our results for experiments.

DOI: 10.1103/PhysRevE.70.031905 PACS number(s): 87.16.Ac, 05.65.+b, 47.54.+r, 87.16.Ka

I. INTRODUCTION

The mitotic spindle in a dividing eukaryotic cell is comprised of several millions of interacting protein molecules [1]. Remarkably, these molecular constituents self-organize to yield patterns at the scale of micrometers. The existence of such self-organized nonequilibrium structures at the subcellular scale is a common feature of biological systems. Such structures include the endoplasmic reticulum and the Golgi complex, membrane-bound organelles which participate in intracellular trafficking. They also include the cytoskeleton, a cell-spanning network of polymers such as actin filaments, intermediate filaments, and microtubules [1].

An individual microtubule is a polar object: microtubule ends, labeled as − and +, grow and shrink at different rates [2]. This polarity dictates the direction of motion of a class of molecular motor proteins on microtubules. Motor proteins such as kinesins use energy derived from adenosine triphosphate (ATP) hydrolysis to exert forces and to translocate along microtubules [3]. The directed motion of individual molecular motor proteins is thus a nonequilibrium phenomenon.

Experiments on centrosome-free fragments of the cytosol containing both motors and microtubules obtain self-organized radial structures called asters [4]. Single asters, in addition to other complex patterns such as vortices, disordered aster-vortex mixtures, and lattices of asters and vortices, are also seen *in vitro*, in experiments on mixtures of molecular motors and microtubules [5]. Features of mitotic spindle formation are reproduced in mixtures of motors, microtubules, and gold beads coated with DNA [6]. The fact that such experiments are able to mimic the complex self-organized states seen in living cells indicates that simple mesoscale models which work with fewer components may be useful in capturing some aspects of cellular pattern formation [7]. In this context, Nédélec and collaborators have studied pattern formation in mixtures of complexes of conventional kinesins with microtubules in a confined quasi-two-dimensional geometry [5]. The later experiments of Surrey *et al.* investigate pattern formation in larger systems where the effects of boundaries appear negligible [8]. The experiments are supplemented by simulations which reproduce many features of the experiments [5,8–11]. The theoretical work described in this paper addresses the modeling of these experiments.

This paper presents a theory of pattern formation in mixtures of molecular motors and microtubules in a confined geometry. We motivate and numerically solve hydrodynamic equations of motion for a coarse-grained field representing the local orientation of microtubules as well as for local motor density fields [12]. In our theoretical description, as well as in the experiments, microtubules are oriented by complexes of bound motors, yielding patterns at large scales [13].

---

*Present address: Department of Physics, University of Illinois at Chicago, 845 W. Taylor St., Chicago, IL 60607-7059, USA. Email address: sumithra@nic.edu

†Email address: menon@imsc.res.in

‡Email address: sunil@physics.iitm.ac.in

1539-3755/2004/70(3)/031905(18)/$22.50

Our approach is closest in spirit to that of Lee and Kardar (LK) [14]. The LK model is a hydrodynamic description of two coupled fields. One of these is a two-dimensional vector field describing the coarse-grained orientation of the microtubule. The other is a conserved scalar field representing the local motor density. The LK model captures two prominent features of the experiments of Nédélec *et al.*: the presence of stable vortices formed by microtubules and the instability of an aster formed in the early stages of pattern formation to a single, stable vortex at large motor densities.

However, despite this success of the LK model, several features of the experiments are incompletely understood. The transition between a single aster and a single vortex seen in the experiments appears to be driven primarily by confinement effects in small systems. In the LK model, confinement does not appear to play a vital role, and the single aster to single vortex transformation is a generic feature even for large system sizes, at large motor densities. Experiments obtain a variety of stable steady states on large systems as a function of motor density. These include a "lattice of asters" state in which asters are the only stable structures, a "lattice of vortices" state, in which individual vortices are stable while asters are absent, as well as an intermediate "aster-vortex mixture" state. The LK approach predicts that a single vortex should be the stable state at large motor densities even for very large systems. Experiments, however, always see a "lattice of asters" in this regime.

The LK model predicts that motor density profiles in asters are always simple decaying exponentials, independent of the rates at which motors hop on and off the filament. However, experiments and theoretical work suggest more complex decays. Such decays include the intriguing possibility of power laws with exponents which vary continuously as a function of the on-off hopping rates. Nédélec, Surrey, and Maggs (NSM) derive equations for motor profiles around a single preformed aster, showing analytically that such profiles are pure power law in nature [15]. The NSM equations describe a *single* aster configuration composed of a fixed number of inward (or outward) pointing microtubules. As a consequence, the density of microtubule *decreases* radially outward from the aster core.

The NSM equations describe motors as either freely diffusing in the solvent or bound to and moving along a microtubule. These states are allowed to interconvert. Since the free motors become bound only in the presence of a microtubule, the conversion rate should be proportional to the local microtubule density. This yields a nontrivial space dependence for this conversion rate, which is responsible for a power-law decay of motor densities predicted by NSM. However, NSM do not address issues of pattern formation. In the NSM model the densities of bound and free motors are governed by separate equations. LK, in contrast, use a single equation for the full motor density field which is effectively the "sum" of these equations, but ignore the dynamics of the difference field.

We suggest here, in contrast to NSM, that at the length scales appropriate to a coarse-grained hydrodynamic description of pattern formation and at the densities of microtubules in the experiments, it is appropriate to ignore fluctuations in the local density of microtubule. The relevant fluctuating field is then the *orientation* field for the microtubule at fixed density, as in the LK model [16,17].

Detailed information regarding the ordering of microtubules in the presence of molecular motors has come from the extensive simulations of Nédélec and collaborators [5,8–10]. These simulations, performed in a two-dimensional geometry, obtain asters and vortices, in addition to relatively disordered configurations in which both asters and vortices are present. However, the best simulations require as many as 19 parameters to be specified; these include fluid viscosities, motor diffusion constants, binding strengths, and microtubule bending rigidities. The uncertainties in these parameters are fairly large, often of an order of magnitude or more; it is unclear which of them are crucial to pattern formation and which others play a secondary role. In contrast, the hydrodynamic approach of this paper uses far fewer parameters, thus enabling efficient scans of parameter space [18–21].

We summarize our results here. In a regime of parameter space for our model which is closest to that for the LK model, we obtain a single vortex as a stable final state for large motor densities. Our results here coincide with the LK results. However, in other regimes, asters are favored. A "lattice of asters" state is stabililized in our model through a low-order relevant term in the equation of motion for the microtubule orientation. On small systems, constraints due to confinement favor a small number of asters, whose number can be increased systematically as parameters are varied.

We calculate the distribution of free and bound motors in asters and vortices obtained in our model. Our results for motor profiles about asters differs from both the LK result and the NSM one. We derive an exponential decay of bound motor densities away from aster cores, modulated by a power law in which the exponent of the power law depends in a nonuniversal way on dynamical parameters. The associated decay length for the exponential can become very large in some regimes of parameter space, yielding what would appear to be pure power-law decays close to the aster core. For vortices, we obtain results equivalent to the LK results.

We obtain, numerically, the solutions to our equations when "crowding" effects due to the interactions of motors moving on microtubules are accounted for in a simple way. Such effects distribute the motor density more uniformly along the microtubules. We argue that the inclusion of such "crowding effects" should further act to favor asters over vortices in finite systems. We adduce simulational evidence for spiral structures favored by confinement and point out that the microtubule configurations seen in experiments do resemble spirals in many cases.

We discuss in some detail the nature of pattern formation in systems where the effects of boundaries can be neglected. Our model generates all the patterns seen in experiments, such as the aster-vortex mixture, the "lattice of asters," and the "lattice of vortices" [22]. We show how these states are linked in the nonequilibrium "phase diagram" of Fig. 1, demonstrating how smooth trajectories in parameter space can connect the states observed, in agreeement with the experiments [23]. Figure 1 is relevant to experimental data in that it shows how a relatively small number of parameters may suffice to fix the macroscopic state of the system.

The outline of this paper is the following. In Sec. II, we describe the details of our model. Section III presents results

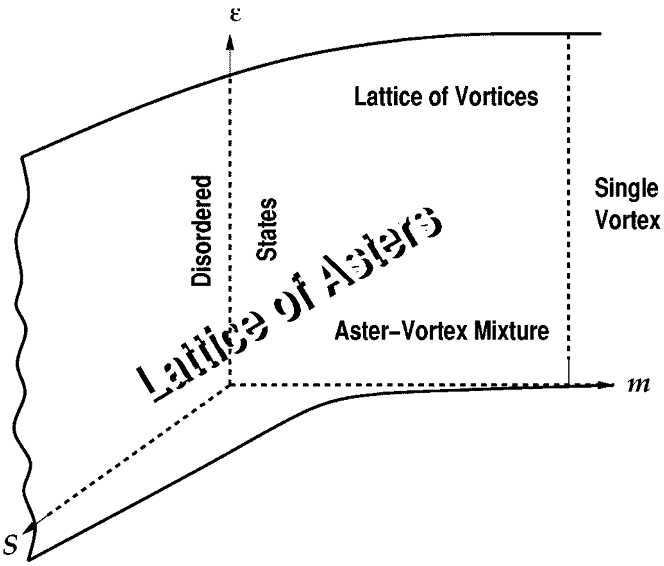

FIG. 1. Qualitative map of steady states, illustrating how different states, the disordered state, the aster-vortex mixture state, the lattice of vortices state, the single vortex, the lattice of asters, dominate in different regimes of parameter space; for a definition of parameters see text. The parameter ϵ is plotted on the y axis, with the total motor density m plotted on the x axis. The parameter S extends out of the ϵ-m plane. Of the states shown, the lattice of asters is obtained generically for nonzero S (out of the plane of the figure), whereas the other states are associated with the $S=0$ plane, although they appear to survive provided S is small enough.

from our numerical simulation of the equations of motion for different boundary conditions. (Our simulation techniques are described in an appendix.) We present results for systems in which the effects of confinement are important as well as for large systems, where confinement is irrelevant and the boundary conditions may be changed without affecting the patterns which form in the bulk. In Sec. IV, we present analytic and numerical results for the profile of motor densities in single vortex and aster configurations. Section IV also discusses how saturation effects resulting from the interactions of bound motors affects motor density profiles. Section V combines the results of Secs. III and IV in a discussion of the relative stability of aster and vortex configurations. We provide a simple argument for the stability of different patterns as parameters in our model are changed. The concluding section, Sec. VI, summarizes the results of this study and outlines possibilities for further work.

II. MODEL

Our model treats motors attached to microtubules differently from motors which diffuse freely in solution. Motors which move on microtubules are referred to as "bound" motors, while those which diffuse in the ambient solvent are referred to as "free" motors. These are described by coarse-grained fields denoted by m_b and m_f, respectively, and obey different equations of motion. In the absence of interconversion terms changing a bound motor to a free motor, m_b obeys a continuity equation involving the current of motors transported along the microtubules. The free motor field m_f obeys a diffusion equation with a diffusion constant D. These two fields are coupled through mechanisms which convert "free" motors to "bound" motors, and vice versa. The equations they obey have the form

$$\partial_t m_f = D\nabla^2 m_f - \gamma'_{f\to b} m_f + \gamma'_{b\to f}\, m_b, \qquad (1)$$

$$\partial_t m_b = -A\,\nabla\cdot(m_b\mathbf{T}) + \gamma'_{f\to b} m_f - \gamma'_{b\to f}\, m_b. \qquad (2)$$

$\gamma'_{b\to f}$ and $\gamma'_{f\to b}$ are the rates at which free motors become bound motors ("on" rate) and vice versa ("off" rate). These rates have dimensions of inverse time. Note that the *total* motor density field $m=m_b(r)+m_f(r)$ is a conserved field.

The term $A\nabla\cdot(m_b\mathbf{T})$ describes the motion of bound motors along microtubules with velocity A. While the rate $\gamma'_{f\to b}$ should depend on the local density of microtubules, we will assume that microtubule density fluctuations are suppressed at the scales relevant to a hydrodynamic description and retain only the orientational degree of freedom of the local microtubule field. We work in two dimensions throughout, since the experiments were performed in a quasi-two-dimensional geometry [13].

The dynamics of the microtubules, given by the equation below, incorporates the terms used by Lee and Kardar in specific limits. It also includes one additional term. As in the LK model, we ignore fluctuations in the density of microtubules, concentrating on their orientational degrees of freedom. The hydrodynamic equation includes terms which reflect the dynamics of individual microtubules. We take these to be stabilized at unit length. It also includes motor-independent and motor-dependent orientation terms. In principle, for a nonequilibrium problem, all symmetry allowed terms must figure here. Of these terms, we will incorporate only the lowest-order symmetry allowed terms whose contributions can be justified transparently on physical grounds.

Our equation then reads

$$\partial_t\mathbf{T} = \mathbf{T}(\alpha - \beta T^2) + \gamma m_b\nabla^2\mathbf{T} + \gamma'\,\nabla m_b\cdot\nabla\mathbf{T} + \kappa'\nabla^2\mathbf{T} + S'\,\nabla m_b. \qquad (3)$$

The first term $\mathbf{T}(\alpha-\beta T^2)$ governs the stabilization of the microtubules at a preferred length of α/β, which we will normalize to unity. The second and third terms $\gamma m_b\nabla^2\mathbf{T}+\gamma'\nabla m_b\cdot\nabla\mathbf{T}$ are alignment terms, reflecting the alignment of microtubules due to the action of bound motors. The third term is also interpretable as a "convective" term, in which the local velocity which convects fluctuations in the $\mathbf{T}$ field is proportional to the gradient of bound motor density.

The fourth term $\kappa'\nabla^2\mathbf{T}$ describes an intrinsic stiffness against distortions, allowing tubules to form an ordered phase in the absence of thermal noise, even at zero motor density. Such a term should always be present in thermal equilibrium, although the experiments indicate that its effects are small at the temperatures at which the experiments are done. The last term is a symmetry allowed term of linear order in the fields. Physically, such a term derives from the tendency of motors to bring initially parallel-oriented microtubules together, creating a nonzero divergence in the local tubule configuration. This term can be derived from a "free energy" term (see Sec. V for a more detailed discussion of this energetics) which favors a net divergence in the tubule configuration. Such physics is a feature of the simulations but is not directly incorporated in the LK model. Note that a few terms allowed by symmetry have been intentionally excluded. These include the term $m_b\nabla(\nabla\cdot T)$; such a term has an effect equivalent to the ∇m_b term of the equation above which is lower order in gradients.

In the LK model the coefficients γ and γ' are taken to be equal. Thus, the second and third terms can be interpreted in terms of the functional derivative of a "free energy" term. In general, however, away from thermal equilibrium, these two coefficients differ and we may explore the regimes of parameter space in which their relative strengths vary. For convenience we choose $\gamma'=\epsilon\gamma$ and vary the parameter ϵ to tune the ratio of these two terms.

The following transformation simplifies the equations considerably: scale length in units of $D/A\sqrt{\beta/\alpha}$, time in units of $\beta D/(\alpha A^2)$, motor density in units of D/γ, and tubule density in units of $\sqrt{\alpha/\beta}$. The equations then reduce to

$$\partial_t m_f = \nabla^2 m_f - \gamma_{f\to b} m_f + \gamma_{b\to f}\, m_b, \tag{4}$$

$$\partial_t m_b = -\ \boldsymbol{\nabla}\ \cdot(m_b \mathbf{T}) + \gamma_{f\to b} m_f - \gamma_{b\to f}\, m_b, \tag{5}$$

$$\partial_t \mathbf{T} = C\mathbf{T}(1 - T^{\,2}) + m_b\nabla^2\mathbf{T} + \epsilon\,\boldsymbol{\nabla}\, m_b \cdot\ \boldsymbol{\nabla}\,\mathbf{T} + \kappa\boldsymbol{\nabla}^2\mathbf{T} + S\,\nabla\, m_b. \tag{6}$$

The parameter C given by $\beta D/A^2$ is the growth constant. $\gamma_{f\to b}$ and $\gamma_{b\to f}$ are scaled in units of inverse time. κ' is appropriately scaled to $\kappa=\kappa'/D$ and $S=S'(\beta D)/(\alpha\gamma A)$. Note that the scaled equations for the free and bound motors [Eqs. (4) and (5)] are invariant when the motor densities are multiplied by a constant. We will use this invariance in Sec. IV C to compare analytic results for motor density profiles with results from numerical simulations.

We relate our scaled parameters to typical experimental values in the following way. The tubule density, scaled in terms of $\sqrt{\alpha/\beta}$, is chosen to be unity. The diffusion constant D is about 20 μm^2/s and $A\sim 1$ μm/s, defining basic units of length and time as 20 μm and 20 s, respectively. A tubule density of 1 implies that over a coarse-graining length of 400 μm^2, there are around 400 microtubules, a value close to that used in the simulations [8]. Our choice for $\gamma_{f\to b}$ and $\gamma_{b\to f}$ corresponds to physical rates of 0.005 s^{-1} to 0.05 s^{-1}, slightly smaller than those in the simulations [10]; using larger rates does not affect our conclusions here.

III. RESULTS AND DISCUSSION: NUMERICAL

A. Confined systems

This section presents the results of our simulations in different regimes of parameter space for the boundary conditions discussed above. The simulations discussed here are on systems of size $L=30$, corresponding to physical length scales of about 60 μm. Our results on somewhat larger systems ($L=50$) are intermediate in character between the results for $L=30$ presented here and our results on systems of much larger sizes ($L\geqslant 100$), where boundary effects are negligible.

The configurations of most relevance to our discussion are asters, vortices, and configurations intermediate between the two, referred to here as spirals. An aster configuration is the unit vector field described as $\mathbf{T}=-\hat{\boldsymbol{r}}$, describing a radial configuration of inward pointing unit vectors. A vortex, on the other hand, is descibed by $\mathbf{T}=\hat{\boldsymbol{\theta}}$. A spiral configuration is described by the unit vector field $\mathbf{T}=T_r\,\hat{\boldsymbol{r}}+T_\theta\hat{\boldsymbol{\theta}}$ in which T_r and T_θ take the forms

$$T_r = -\cos(\alpha), \quad T_\theta = \sin(\alpha), \tag{7}$$

where α is a constant. This contains both asters and vortices in appropriate limits: In the limit $\alpha=0$, this equation describes an aster, while in the limit $\alpha=\pi/2$, the configuration is a vortex. Thus asters and vortices are particular limiting cases of more general spiral states.

We work at a fixed large motor density of $m=m_b+m_f=0.5$. We work at fixed values of $\gamma_{b\to f}=\gamma_{f\to b}=0.5$ here but have checked that making the motors more or less processive does not alter our results qualitatively. For motors with very small "on" and "off" rates, we see disordered states best described as aster-vortex mixtures. The patterns obtained here emerge at still higher motor densities for low values of the processivity. We work with a small value of κ ($\kappa=0.05$ here), such that the magnitude of the self-alignment term $\kappa\nabla^2\mathbf{T}$ is small compared to $m_b\nabla^2\mathbf{T}$.

1. *Reflecting boundary conditions*

Our results for reflecting boundary conditions are shown in Figs. 2(a)–2(d). Each column represents a different value of S, i.e., (a) $S=0$, (b) $S=0.05$, (c) $S=0.5$, and (d) $S=2$. We vary the parameter ϵ in these scans, with ϵ taking the values $\epsilon=0.0$, 0.5, 1.0, and 5 as shown.

In Figs. 2(a)–2(d), the effects of varying ϵ with reflecting boundary conditions are the following. In Fig. 2(a), $S=0$ and the steady state configuration at $\epsilon=0$ is an aster with tubules directed radially inward toward the core. When ϵ is increased to 0.5, the configuration resembles a "spiral." As ϵ is increased further the spiral distorts into a vortex. In Fig. 2(b), we show configurations at small but nonzero S, $S=0.05$. The single aster is stable for $\epsilon=0$ and 0.5, but yields to a single vortex for larger ϵ. A general observation is that the core of the vortex is increasingly distorted as ϵ is increased further.

Figure 2(c) shows steady state configurations at $S=0.5$. A tendency toward the formation of a lattice of asters is apparent, as ϵ is increased at these values of S. This is consistent with our earlier results on large systems, where we observed that nonzero S always promoted the lattice of asters. At large ϵ, e.g., $\epsilon=5$, there is a pronounced tendency toward alignment, yielding a steady state pattern of a vortex with a highly distorted core. Figure 2(d) shows configurations at $S=2$, where the lattice of asters is present at all values of ϵ shown. At large ϵ, the tendency toward parallel alignment competes with the tendency toward aster formation. At still larger values of ϵ, we obtain an aligned phase in the bulk (not shown), reminiscent of the "bundles" seen in the experiments at large motor concentration.

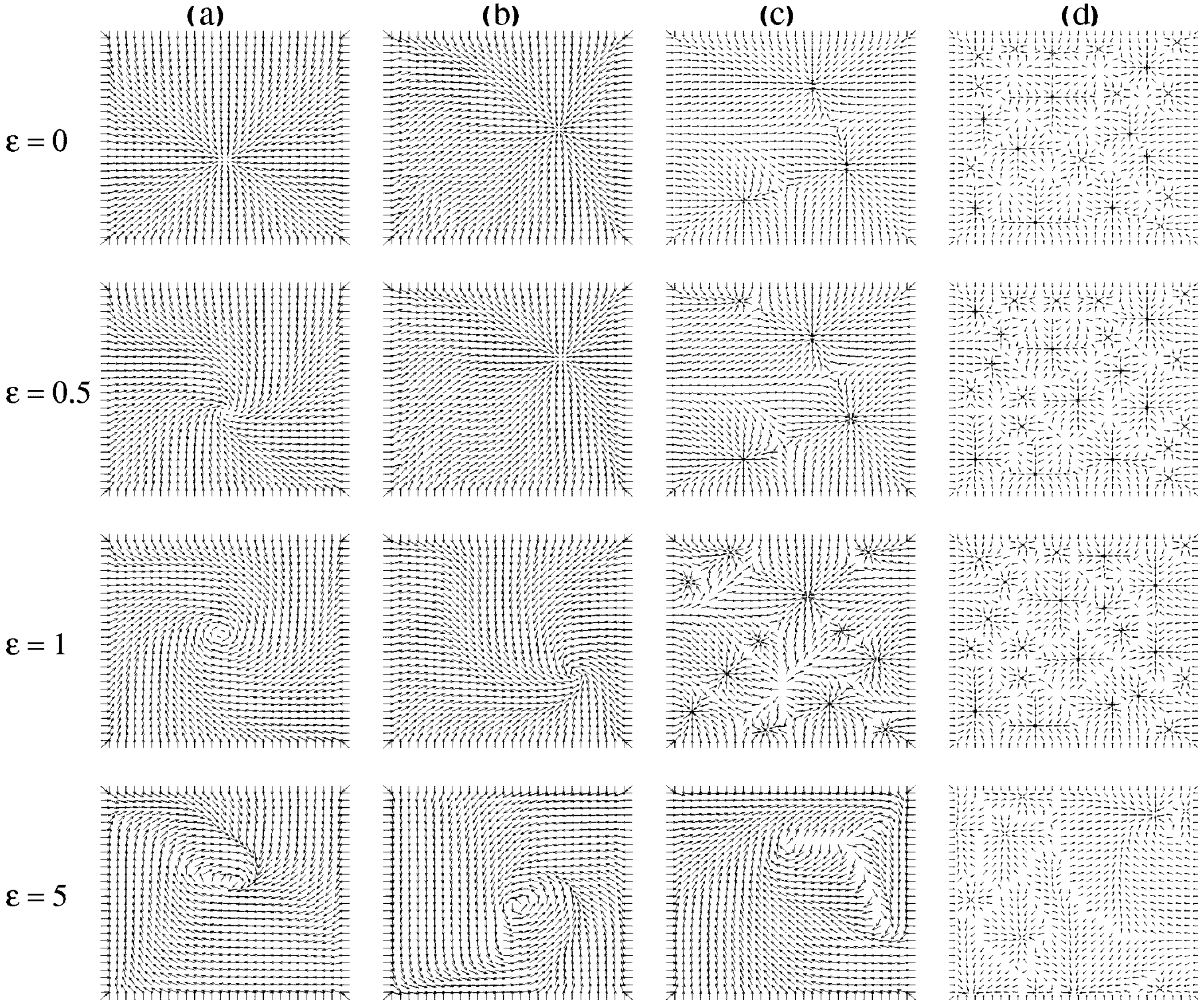

FIG. 2. Steady-state configurations of microtubules with reflecting boundary conditions. The parameters are $m=0.5$ and $\gamma_{f\to b}=\gamma_{b\to f}=0.5$. Patterns are shown at different ϵ at (a) $S=0$, (b) $S=0.05$, (c) $S=0.5$, and (d) $S=2$.

Figures 3(a)–3(d) show bound motor density profiles corresponding to the microtubule arrangements of Figs. 2(a)–2(d). Lighter regions of the figure indicate regions of larger density. Note that the bound motor density is concentrated at the centers of asters. In vortex configurations, the motor density profiles for bound motors are far smoother. In the “lattice of asters” configuration, the bound motor density profiles peaks at the centers of the asters, decaying to a small value at intermediate points far away from aster cores. The profiles of free motor densities are visually very similar to those for bound motors and are not shown here.

2. Parallel boundary conditions

We now discuss pattern formation in finite systems with parallel boundary conditions [see Figs. 4(a)–4(d)]. These are to be contrasted with Figs. 2(a)–2(d). Note that qualitatively different sequences of patterns are stabilized at identical values of other parameters, depending on the boundary conditions. This illustrates the sensitivity to boundary conditions which obtains for sufficiently small system sizes L.

Figure 4(a) shows pattern formation with parallel boundary conditions at $S=0$. A single vortex is obtained as a steady state at all values of ϵ shown, i.e., $\epsilon=0.0$, 0.5, 1.0, and 5. Figure 4(b) shows patterns for $S=0.05$. The steady state here is a single aster with tubules pointing *outward* at the core, but aligned with the configurations at the boundary. (We term such configurations as “outward asters.”) Clearly these arise as a consequence of the boundary conditions which favor vortices and the parameter regime which favors asters. At $\epsilon=5$, the steady state is a well-formed, clean vortex. Figure 4(c) illustrates pattern formation at $S=0.5$, as a function of ϵ. We see a tendency toward the formation of the lattice of asters phase expected for large S for sufficiently large ϵ, although indications of this are seen even for small ϵ.

At very high ϵ, we obtain an unusual configuration which we term a “flag.” In this configuration, tubules point radially outward near the core while merging with the imposed par-

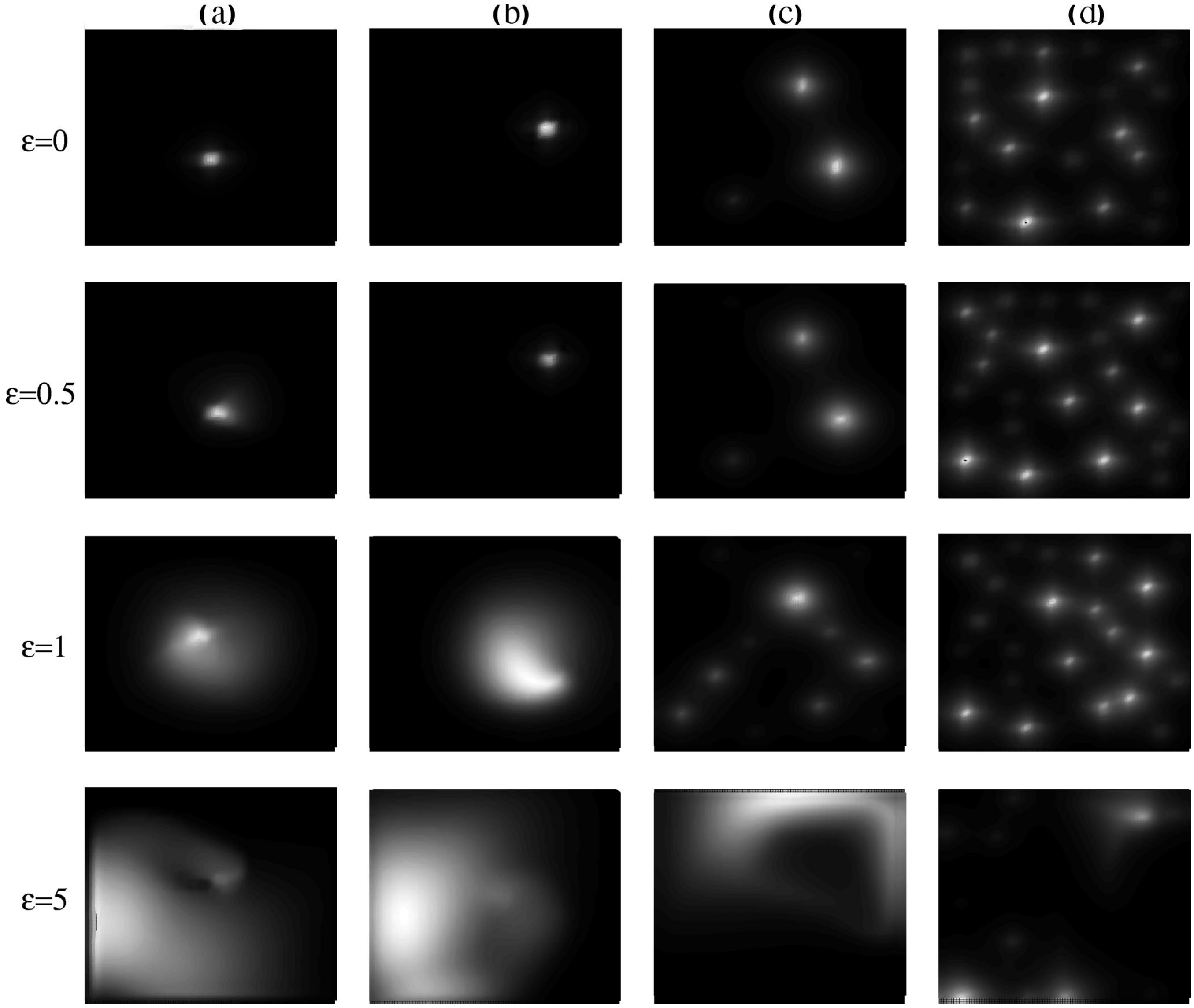

FIG. 3. Steady state bound motor density profiles with reflecting boundary conditions. The parameters are $m=0.5$ and $\gamma_{f\rightarrow b}=\gamma_{b\rightarrow f}=0.5$. Profiles are shown at different ϵ at (a) $S=0$, (b) $S=0.05$, (c) $S=0.5$, and (d) $S=2$. The darker regions indicate regions of lower motor density.

allel microtubule configuration near the boundary. However, the configuration appears to have a fourfold axis, in which the axis lines are along the diagonal. Across this axis, the microtubule orientation changes sharply. This fourfold symmetry reflects the fourfold symmetry of the simulation box. Finally, Fig. 4(d) shows patterns formed at $S=2$. In this regime, the lattice of asters is the stable steady state for all values of ϵ.

Figures 5(a)–5(d) show bound motor density profiles corresponding to the microtubule arrangements of Figs. 4(a)–4(d). Note that the density distribution in single vortices varies smoothly, consistent with theoretical expectations. The profiles appear sensitive to the boundary and a fourfold rotation axis can be seen in several of the patterns which involve a single vortex. The patterns for nonzero and large S are very similar to those obtained for reflecting boundary conditions with similar values of parameters. The profiles of free motor densities are again visually very similar to those for bound motors and are not shown here.

3. Discussion

Our results for the cases outlined in the preceding subsection are summarized as follows. For reflecting boundary conditions, we obtain the general sequence aster →spiral→ vortex at $S=0$. This sequence is obtained at fixed motor density, as a function of the nonequilibrium parameter ϵ. With parallel boundary conditions, the patterns formed are generically vortices, although the region surrounding the core is progressively distorted as ϵ is increased. Finite S favors the formation of a lattice of asters, as in large systems. We observe some unusual configurations such as the “flag” configuration, reflecting the fourfold symmetry of the simulation box and the outward aster.

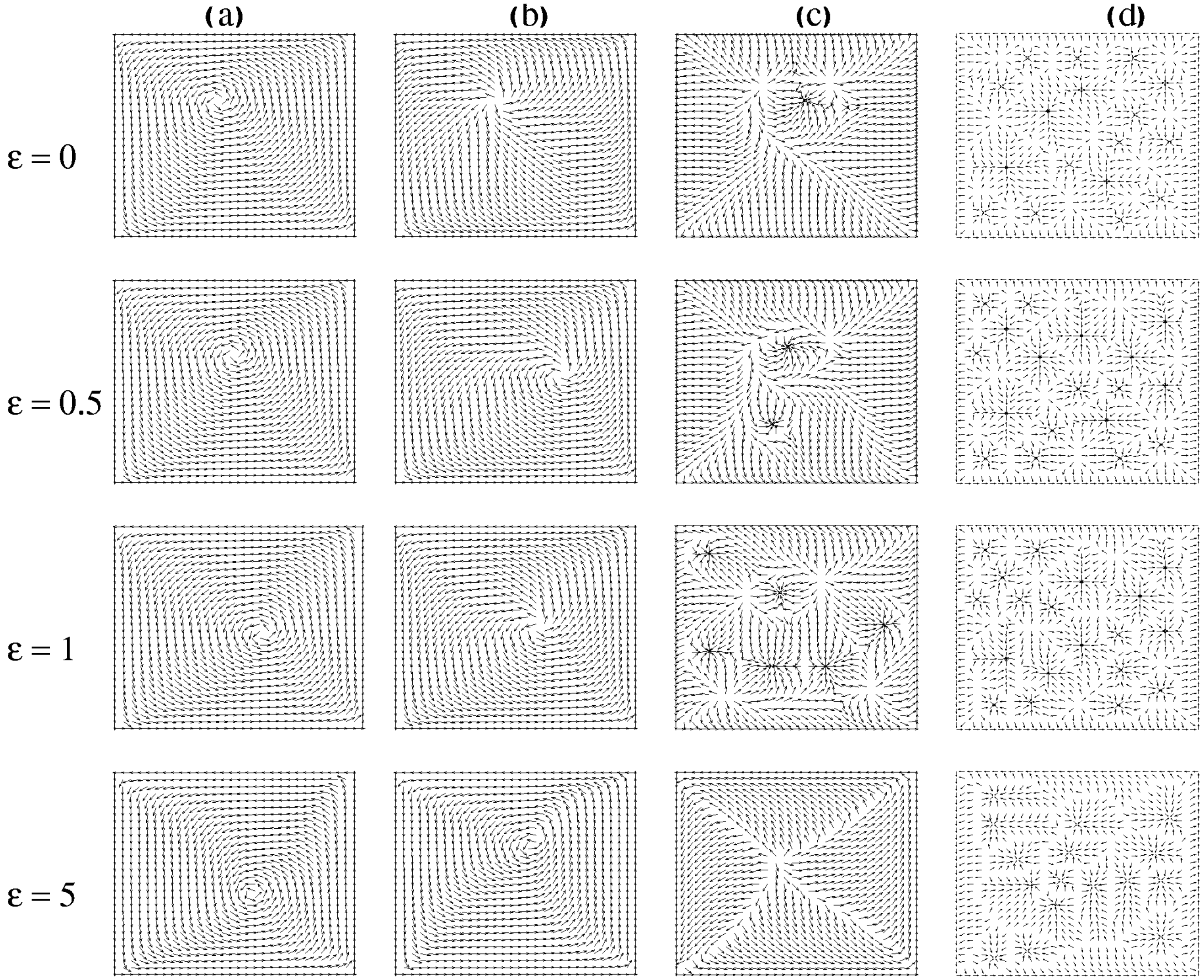

FIG. 4. Steady state configurations of microtubules with parallel boundary conditions. The parameters are $m=0.5$ and $\gamma_{f\to b}=\gamma_{b\to f}=0.5$. Patterns are shown at different ϵ at (a) $S=0$, (b) $S=0.05$, (c) $S=0.5$, and (d) $S=2$.

In our simulations, spirals arise as a consequence of the competition between the vortex configurations favored locally for intermediate and large values of ϵ and reflecting boundary conditions, which favor asters. Spirals offer the best compromise between these and it is reasonable to expect that such states should be more generically seen than either asters or vortex states. Indeed, inspection of the configurations associated with the "lattice of vortices" in Ref. [8] provides strong visual evidence for generic spiral states.

The bound and free motor profiles we obtain in the simulations are consistent with expectations from our theoretical analysis (see below). The characteristic sharp peaks in motor density profiles associated with asters are replaced by far more slowly varying profiles for vortices. The lattice of asters, therefore has strong signals in the motor distribution function. Appropriate experimental labeling of motors in this phase should yield patterns and profiles closely similar to those displayed here.

We have also examined the effects of varying κ, the motor-independent self-alignment term for microtubules. (While the value of κ appears to be too small in the experiments to significantly affect pattern formation—there seems to be no evidence that motor-independent alignment occurs—we find that using small values of κ helps us to generate somewhat smoother patterns.) As expected physically, for large κ (=5.0) with both reflecting and parallel boundary conditions, a phase which has tubules aligned along a particular direction is formed at all ϵ and S values. The lattice of asters does not appear here. At $\kappa=0.5$, with reflecting boundary conditions, the lattice of asters phase appears at sufficiently large S. With parallel boundary conditions, a single vortex appears at low ϵ and $S=0$, which transforms into the lattice of asters phase at high S. In summary, the κ term competes with the motor-density-dependent alignment terms; in regimes in which it dominates, it favors parallel alignment of microtubules leading to a pattern consistent with the boundary conditions. The effects of such a term may be more noticeable in experiments performed at significantly higher densities of microtubule than have been attempted so far.

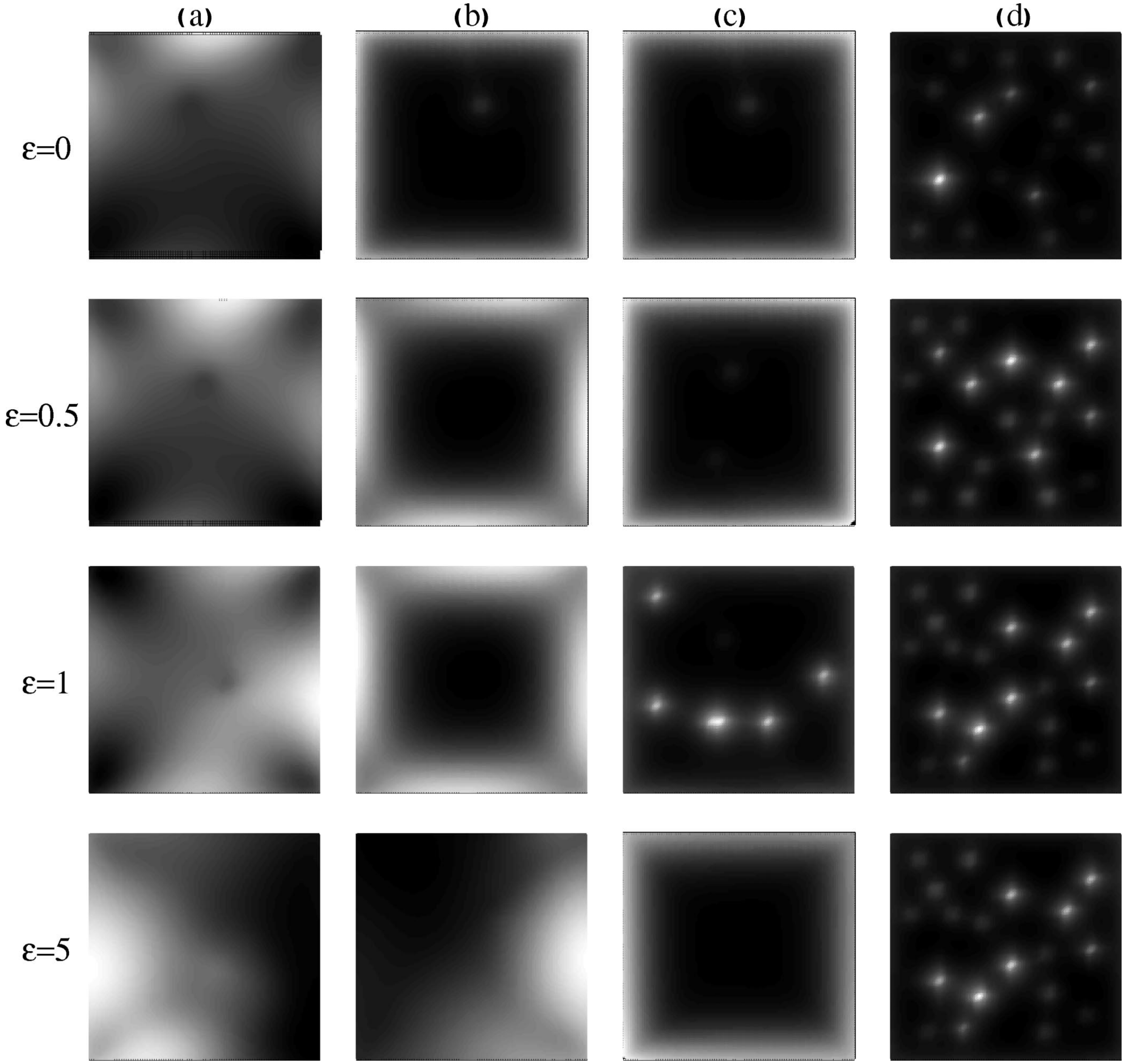

FIG. 5. Steady state bound motor density profiles with parallel boundary conditions. The parameters are $m=0.5$ and $\gamma_{f\rightarrow b}=\gamma_{b\rightarrow f}=0.5$. Profiles are shown at different ϵ at (a) $S=0$, (b) $S=0.05$, (c) $S=0.5$, and (d) $S=2$. The darker regions indicate regions of lower motor density.

B. Pattern formation in large systems

This section presents the results of our simulations in different regimes of parameter space on large systems than those discussed above. These simulations are on systems of size $L=100-200$, corresponding to physical length scales of about $200-400$ μm. In these systems, generically, the nature of the patterns formed appears to be independent of the boundary conditions used whether such boundary conditions are parallel, reflecting, or random. We may thus summarize our results in a nonequilibrium "phase diagram" (Fig. 1), illustrating the nature of patterns formed as our three main parameters m, ϵ, and S are varied.

Figures 6(a)–6(d) depict four stable configurations obtained in different regimes of parameter space for an $L=100$ lattice. Figure 6(a) shows a disordered arrangement of microtubules obtained at very low motor densities ($m=0.005$) with $\epsilon=0.5$ and $S=0$. Figure 6(b) shows an aster-vortex mixture obtained at $m=0.01$ at the same values of ϵ and S. Note the presence both of well-formed asters and of vortices in the configurations. This figure is to be contrasted to Fig. 6(c), obtained at $m=0.05$, taking $\epsilon=5$ and $S=0.001$. Note the absence of asters in this regime of parameter space. Finally, Fig. 6(d), obtained with $m=0.5$, $\epsilon=1$, and $S=1$, illustrates a lattice of asters, with asters being the only stable defects present. We can vary the sizes and numbers of asters obtained in configurations such as the one shown in Fig. 6(d), by changing S. A larger S yields a large number of

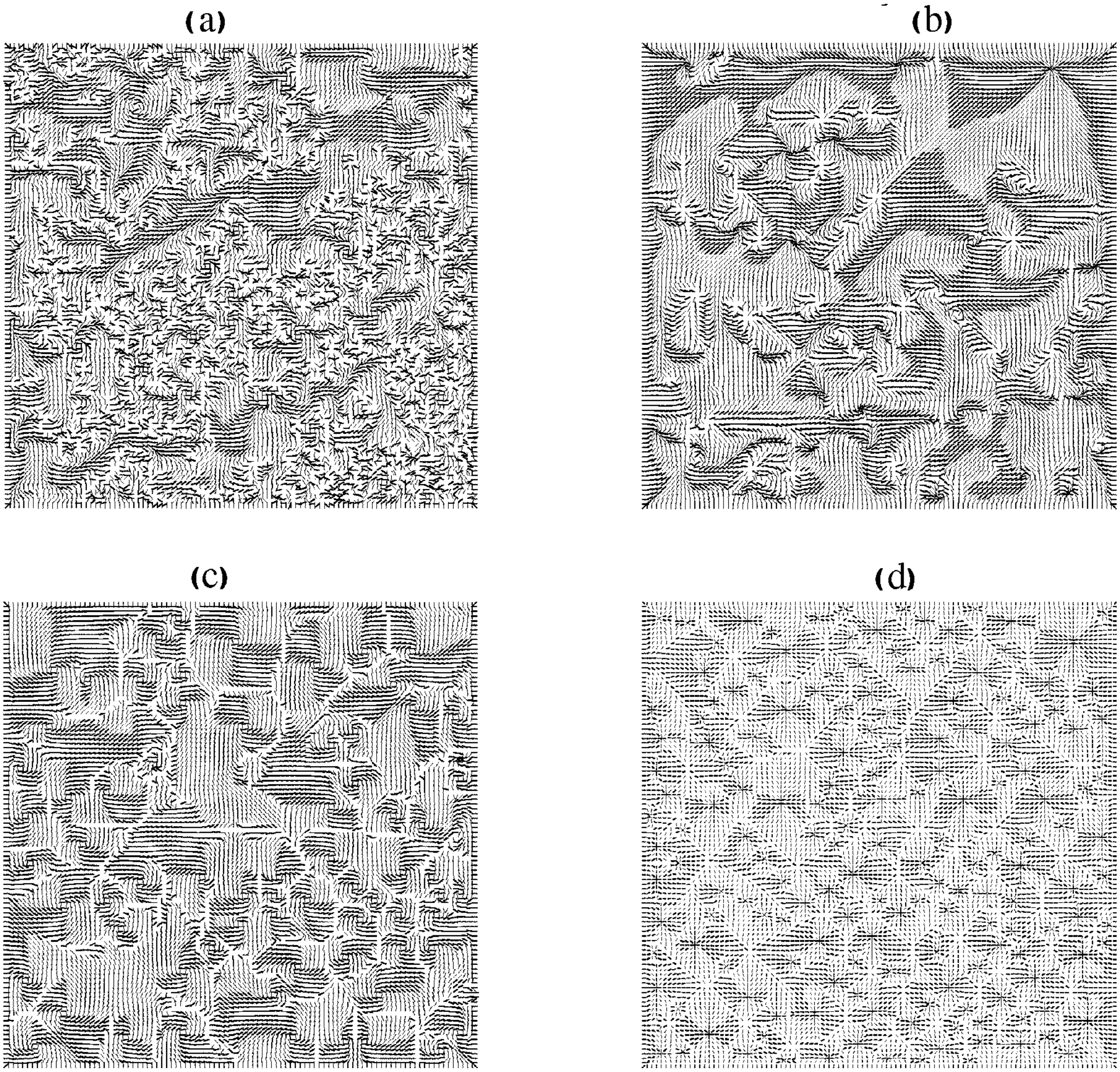

FIG. 6. Steady state configurations in our model at different parameter values (see text): (a) Disordered states obtained at very low motor densities ($m=0.005$ $\epsilon=0.5$ and $S=0$); (b) aster-vortex mixture obtained at ($m=0.01$, $\epsilon=0.5$ and $S=0$); (c) lattice of vortices at ($m=0.05$, $\epsilon=5$ and $S=0.001$); (d) lattice of asters obtained at ($m=0.5$, $\epsilon=1$ and $S=1$).

small asters, while smaller values of S yield a smaller number of large asters [15].

Our results are summarized in Fig. 1 which shows the states that dominate in the three-dimensional space spanned by ϵ, S, and m. For $S=0$, we obtain aster-vortex mixture states at low motor density, which become a lattice of vortices at somewhat higher motor densities. Large values of $\epsilon\,(\epsilon\geqslant 1)$ yield well-formed vortexlike configurations while small ϵ yields structures better described as aster-vortex mixtures. At intermediate values of ϵ and m, spirals rather than vortices appear to dominate. At large m, with $S=0$ and large ϵ, a single vortex is obtained [14].

For nonzero but small S, these states appear to continue out of the $S=0$ plane but are rapidly replaced by a lattice of asters for larger S. A cut of Fig. 1 at finite S yields disordered states at small m and a lattice of asters at larger m. We can thus understand the sequence of patterns formed upon increasing m in mixtures of kinesin constructs with microtubules in terms of a trajectory which begins in the $S=0$ (or S sufficiently small) plane in the disordered phase and transits between the aster-vortex mixture and the lattice of vortices (both of which lie in this plane) as m is increased. As m increases further and the effects of the S term become important, such a trajectory moves out toward nonzero S, encountering the lattice of asters.

We have also examined the effects of changing the motor processivity, a quantity proportional to the ratio of $\gamma_{f\to b}$ to $\gamma_{b\to f}$. Smaller values of this ratio are appropriate to molecular motors such as nonclaret disjunctional (NCD). At $\gamma_{f\to b}=0.005, \gamma_{b\to f}=0.05$, we find that the disordered regime shown in Fig. 1 expands, so that at equivalent values of m disordered states occupy much of the domain associated previously with the lattice of vortices. Whereas kinesins follow the sequence disordered – lattice of vortices–aster-vortex mixture–lattice of asters as m is increased, a mixture of microtubules with NCD motors bypasses the lattice of vortices altogether, transiting directly from the disordered state to the lattice of asters in the experiments [8]. In terms of Fig. 1, the expanded regime of disordered states for the NCD motor suggests that patterns such as the lattice of vortices and the aster-vortex mixture may be inaccessible at the motor densities at which the experiments are done, since the effects of the S term might be expected to dominate at large m.

Discussion

A large number of disordered steady states are seen in the simulations. Physically, these states arise because the dominant contribution to the stiffness to distortions in the T field comes from the motors; it is low in regions depleted of motor density and large in regions where many motors are present. Since bound motors are convected along the local tubule direction, large inhomogeneities in the local motor density occur in the final steady states (such as in the "core" of the asters), with the precise character of the final configuration dependent on the initial condition. Such "arrested" states have also been discussed in other contexts earlier, as well as in this particular one by Lee and Kardar [14]. Thus, it is natural that the patterns obtained at low motor densities should then be inhomogeneous and disordered, and that a large number of steady states should thus be generated, depending on the initial pattern of microtubules and of motors.

We now comment on the topological attributes of the patterns we observe, since asters and vortices are conventionally thought of as topological objects. We stress the following point: Describing configurations usefully in terms of smooth and singular (topological) deformations presupposes a uniform minimum energy state. To ensure this, the "spin stiffness" or equivalently the elastic cost for deformations must be nonzero. In this problem, the local motor density provides the dominant contribution to the stiffness. In regions where such motor densities are either low or vanish altogether, or where weak noise is sufficient to suppress local ordering, there is simply no penalty for making arbitrary deformations in the microtubule field. A second difficulty with a purely topological approach to the formation of patterns is that asters and vortices are topologically speaking, entirely equivalent. (Take an aster and rotate all arrows by 90° — a vortex is then generated.) However, the motor density fields associated with asters and vortices are not identical. This provides a mechanism for stabilizing either asters or vortices in different regimes of parameter space, since the motor density fields are also dynamical fields and obey their own respective equations of motion. As regards how these may be distinguished: asters and vortices are represented by local regions in which the coarse-grained microtubule field is either represented by a purely radial unit vector $\hat{\boldsymbol{r}}$ or by a purely tangential one $\hat{\boldsymbol{\theta}}$ respectively. Such configurations have no global topological significance, as explained earlier but can easily be identified locally, either numerically or even visually (as in the experiments), as the pictures of Fig. 6 corroborate.

There are other defects which are also seen in this model. We note that all the defects seen in Fig. 6 can be described by $\theta(\phi)=S\times\phi+C$ in cylindrical polar (r,ϕ) coordinates. Here S is the winding number, +1 for asters (with $C=0$) and vortices (with $C=\pi/2$). All other defects seen in Fig. 6 are obtained by setting $S=-1$ and choosing C in the interval $C=0$ to $\pi/2$. However, it is equally obvious from the figure that certain classes of defects dominate over others and that is precisely what our approximate classification of the different states highlights [25].

IV. ANALYTIC RESULTS FOR MOTOR PROFILES IN ASTER AND VORTEX CONFIGURATIONS

We now present an analytic calculation of free and bound motor density profiles in vortex and aster configurations. We fix single vortex and aster configurations of microtubules and solve for steady state free and bound motor densities in the presence of the fixed microtubule configuration [26].

We find steady state solutions of Eqs. (4) and (5) by setting the time derivatives to zero i.e., $\partial_t m_f=\partial_t m_b=0$. Adding and subtracting these equations, we obtain

$$\nabla^2 m_f - \nabla \cdot (m_b \mathbf{T}) = 0, \tag{8}$$

$$\nabla^2 m_f + (\gamma_{b\to f} m_b - \gamma_{f\to b}\, m_f) = 0. \tag{9}$$

The first of these equations implies that

$$\boldsymbol{\nabla} m_f = m_b \mathbf{T} + \mathbf{C}, \tag{10}$$

where $\mathbf{C}$ is an arbitrary vector whose divergence $\boldsymbol{\nabla}\cdot\mathbf{C}=0$.

A. Single vortex, i.e., $\mathbf{T}=\hat{\boldsymbol{\theta}}$

Assuming radial symmetry, we may write $m_f=m_f(r)$and $m_b=m_b(r)$. Let $\mathbf{C}=c_r\hat{\mathbf{r}}+c_\theta\hat{\boldsymbol{\theta}}$. Equation (8) then implies

$$\partial_r m_f\, \hat{\boldsymbol{r}} = m_b \hat{\boldsymbol{\theta}} + c_r\, \hat{\boldsymbol{r}} + c_\theta \hat{\boldsymbol{\theta}}. \tag{11}$$

Hence,

$$c_r = \partial_r m_f \text{ and } c_\theta = -\, m_b. \tag{12}$$

The constraint of zero divergence for $\mathbf{C}$ yields

$$\partial_r c_r + \frac{c_r}{r} + \frac{1}{r}\partial_\theta\, c_\theta = 0. \tag{13}$$

Since $c_\theta=-m_b(r)$ is purely radial

$$\partial_\theta\, c_\theta = 0. \tag{14}$$

Equation (13) then becomes a radial equation

$$\partial_r c_r + \frac{c_r}{r} = 0. \tag{15}$$

Using $c_r=\partial_r\, m_f$, we obtain

$$\nabla^2 m_f = 0, \tag{16}$$

which supports solutions of the form

$$m_f(r) = c_1 + c_2 \ln(r), \tag{17}$$

where c_1 and c_2 are constants to be determined by boundary conditions and normalization.

Equation (9) now simplifies to

$$\gamma_{b\to f}\, m_b - \gamma_{f\to b} m_f = 0 \tag{18}$$

which yields

$$m_b(r) = \frac{\gamma_{f\to b}}{\gamma_{b\to f}}[c_1 + c_2 \ln(r)]. \tag{19}$$

We must determine the constants c_1 and c_2. There is no radial current of motors (bound or free) in the vortex configuration. The condition of no radial current of free motors at the boundary implies

$$\partial_r m_f(r) = 0 \quad \text{at } r = L, \tag{20}$$

therefore implying that $c_2=0$. The constant c_1 is determined by the normalization

$$\int d^2r[m_f(r) + m_b(r)] = N. \tag{21}$$

In the vortex configuration

$$\int d^2r\left(1 + \frac{\gamma_{f\to b}}{\gamma_{b\to f}}\right)c_1 = N, \tag{22}$$

which gives

$$c_1 = \frac{n}{2\pi}\frac{1}{(1 + \gamma_{f\to b}/\gamma_{b\to f})}, \tag{23}$$

with n the density of motor N/L^2.

The result above holds for purely tangential boundary conditions, consistent with the symmetry of the vortex. It will be modified with respect to the simulation results both as a consequence of the (Cartesian) latticization used to discretize the equations as well as by the fourfold symmetry of the simulation box. Both these factors will lead to a combination of the logarithmic and constant solutions above.

B. Single aster solution, i.e., $\mathbf{T}=-\hat{\boldsymbol{r}}$

We again assume radial symmetry for the bound and free motor densities. We choose $\mathbf{C}=f(r)\hat{\boldsymbol{r}}$, with $f(r)$ such that $\mathbf{C}$ is divergenceless, i.e., $\nabla\cdot\mathbf{C}=0$. We thus obtain $f(r)=c_0/r$, with c_0 a constant. The radial current of free motors is $(-\partial_r m_f)\hat{\boldsymbol{r}}$ while the radial current of bound motors is $(-m_b)\hat{\boldsymbol{r}}$. The boundary condition that the total motor current vanishes at the boundary implies

$$\partial_r m_f + m_b = c_0/r = 0 \quad \text{at } r = L. \tag{24}$$

This ensures that $c_0=0$ and therefore

$$\partial_r m_f(r) = -\, m_b(r). \tag{25}$$

Equation (9) becomes

$$\partial_r^2 m_f + \left(\frac{1}{r} - \gamma_{b\to f}\right)\partial_r m_f - \gamma_{f\to b} m_f = 0. \tag{26}$$

This is a second order differential equation whose solution is completely specified if the value of the function and of its derivative at the boundary are supplied. Given these boundary conditions, the free motor density can be obtained via a numerical solution using the Runge-Kutta method. The bound motor density is also easily determined via a radial derivative of the free motor density.

We now derive exact and asymptotic expressions for motor densities in the aster geometry. The general solution to the equation above is a combination of confluent hypergeometric functions and has the form

$$\begin{aligned} m_f(r) = e^{(\gamma_{b\to f}-\sqrt{\gamma_{b\to f}^2+4\gamma_{f\to b}})r/2}\Bigg[& c_2 F_1\left(\frac{1}{2} - \frac{\gamma_{b\to f}}{2\sqrt{\gamma_{b\to f}^2 + 4\gamma_{f\to b}}},\right. \\ & \left. 1, \sqrt{\gamma_{b\to f}^2 + 4\gamma_{f\to b}}r\right) \\ & + c_1 U\left(\frac{1}{2} - \frac{\gamma_{b\to f}}{2\sqrt{\gamma_{b\to f}^2 + 4\gamma_{f\to b}}}, 1,\right. \\ & \left.\sqrt{\gamma_{b\to f}^2 + 4\gamma_{f\to b}}r\right)\Bigg]. \end{aligned} \tag{27}$$

The functions ${}_1F_1(1/2-\gamma_{b\to f}/2\sqrt{\gamma_{b\to f}^2+4\gamma_{f\to b}}, 1, \sqrt{\gamma_{b\to f}^2+4\gamma_{f\to b}}r)$ and $U(1/2-\gamma_{b\to f}/2\sqrt{\gamma_{b\to f}^2+4\gamma_{f\to b}}, 1, \sqrt{\gamma_{b\to f}^2+4\gamma_{f\to b}}r)$ are the two solutions of the confluent hypergeometric Kummer equation. It is useful to define a quantity p given by

$$p = \frac{1}{2}\left(1 - \frac{\gamma_{b\to f}}{\sqrt{\gamma_{b\to f}^2 + 4\gamma_{f\to b}}}\right). \tag{28}$$

Note that

$$0 \leqslant p \leqslant 0.5, \tag{29}$$

with $\gamma_{b\to f}, \gamma_{f\to b} \geqslant 0$. The argument of the exponent in Eq. (27) is always negative for all $\gamma_{b\to f}, \gamma_{f\to b} \geqslant 0$. The coefficients c_1 and c_2 are determined by boundary and normalization conditions.

The boundary condition is that there is no total motor current at the boundary, i.e.,

$$\partial_r m_f(r) + m_b(r) = 0 \quad \text{at } r = L, \tag{30}$$

since the radial current of bound motors in the aster configuration is $\mathbf{J}=-m_b(r)\hat{\boldsymbol{r}}$. This can be used to determine c_2 in terms of c_1. We find that on imposing the no-current boundary condition, c_2 is very small compared to c_1 and is significant only when the system size is of order the "correlation" length over which the density decays. We will assume (see below) that we can set $c_2=0$ to yield physically admissible solutions.

The constant c_1 can now be fixed by the normalization condition which requires the total number of motors (bound + free) be constant,

$$\int_0^L d^2r[m_b(r) + m_f(r)] = N. \tag{31}$$

where N is the total number of motors.

A physical argument for neglecting the ${}_1F_1(1/2 - \gamma_{b\to f}/2\sqrt{\gamma_{b\to f}^2+4\gamma_{f\to b}}, 1, \sqrt{\gamma_{b\to f}^2+4\gamma_{f\to b}}r)$ term in comparison with the $U(1/2-\gamma_{b\to f}/2\sqrt{\gamma_{b\to f}^2+4\gamma_{f\to b}}, 1, \sqrt{\gamma_{b\to f}^2+4\gamma_{f\to b}}\ r)$ is the following. A power series expansion yields

$$ {}_1F(p,q,x) = \sum_{n=0}^{\infty} \frac{(p)_n}{(q)_n} \frac{x^n}{n!}, \tag{32}$$

where $(p)_n=(p+n-1)!/(p-1)!$ and $(p)_0=1$. This function is a monotonically (exponentially) increasing function of r. Such a density distribution implies a motor density per unit area which increases as r is made arbitrarily large, a solution which is clearly untenable on physical grounds. On the other hand, $U(1/2-\gamma_{b\to f}/2\sqrt{\gamma_{b\to f}^2+4\gamma_{f\to b}},1,\sqrt{\gamma_{b\to f}^2+4\gamma_{f\to b}}r)$ decreases monotonically with increasing r. Hence we retain only the $U(1/2-\gamma_{b\to f}/2\sqrt{\gamma_{b\to f}^2+4\gamma_{f\to b}},1,\sqrt{\gamma_{b\to f}^2+4\gamma_{f\to b}}r)$ part of the solution for $m_f(r)$.

To derive the asymptotics we begin with the integral representation

$$U(p,q,x) = \frac{1}{\Gamma(p)} \int_0^{\infty} e^{-xt} t^{p-1} (1+t)^{q-p-1}\, dt. \tag{33}$$

We relabel $(\sqrt{\gamma_{b\to f}^2+4\gamma_{f\to b}})r=z$ and $\frac{1}{2}(1-\gamma_{b\to f}/\sqrt{\gamma_{b\to f}^2+4\gamma_{f\to b}})=p$ for notational convenience. We then obtain

$$U(p,1,z) = \frac{1}{\Gamma(p)} \int_0^{\infty} \frac{e^{-zt} t^{p-1}}{(1+t)^p} dt. \tag{34}$$

We now change variables to $u=zt$. The integral is then

$$\frac{1}{\Gamma(p)} \frac{1}{z^p} \int_0^{\infty} \frac{e^{-u} u^{p-1}}{(1+u/z)^p} du. \tag{35}$$

Since p is a small number between 0 and 0.5 we may expand the denominator binomially. The first term gives $\Gamma(p)$ and subsequent terms converge. Hence, in the large z limit, the integral is just $\Gamma(p)$. Therefore,

$$m_f(r) = c_1 \frac{e^{-r/\xi}}{(\gamma_{b\to f}^2 + 4\gamma_{f\to b})^{p/2} r^{\,p}},$$

$$m_b(r) = c_1 \frac{e^{-r/\xi}}{(\gamma_{b\to f}^2 + 4\gamma_{f\to b})^{p/2} r^{\,p}} \left(\frac{p}{r} + \frac{1}{\xi}\right),$$

where the inverse of the "correlation" length is defined as

$$\xi^{-1} = \left| \frac{(\gamma_{b\to f} - \sqrt{(\gamma_{b\to f}^2 + 4\gamma_{f\to b})}}{2} \right| = \left| \frac{p\gamma_{b\to f}}{2p-1} \right|. \tag{36}$$

The correlation length ξ and the power-law exponent p depend on $\gamma_{f\to b}$ and $\gamma_{b\to f}$. We see that the bound motor density in the aster case has an exponential fall modulated by a power-law tail instead of the pure exponential falloff predicted in the LK model.

These results can, in principle, be compared directly to the experiments of NSM in Ref. [15], but for one difficulty. Out of the aster configurations generated in the experiments in steady state, NSM specifically *select* those configurations in which the aster densities decay most closely as $1/r$ away from the aster core. This then enables a direct fit to their theoretical predictions. In contrast, the theoretical predictions here are in the limit where the microtubule density profile is constant, so that fluctuations in the density of microtubule can be neglected (see the Introduction for a discussion of this point). Thus, while inserting appropriate numbers for the on-off rates would generate power-law profiles closely resembling those of NSM, at least not too far away from the core, a direct comparison to these particular experiments may not be feasible.

Another limit in which an exact answer can be obtained is the following. If there is no interconversion between the two species of motors (i.e., $\gamma_{b\to f}=\gamma_{f\to b}=0$), the equations of motion for free motors and bound motors decouple. The numbers of free motors and bound motors in the system are then conserved independently. The free motor density equation supports solutions of the form $m_f(r)=c_1+c_2\ln(r)$, where c_1 and c_2 are constants of integration. Imposing a vanishing current of free motors at the boundary constrains $c_2=0$. The other constant c_1 can be fixed from the condition that the total number of free motors is constant. The bound motor density then has the simple power law behavior $m_b(r)\sim 1/r$.

C. Comparison of the analytic results with simulations

These analytic results can now be compared to the results of direct simulations of the dynamical equations for single aster and vortex structures. We choose $\mathbf{T}=\hat{\boldsymbol{r}}$ in the full equations of motion for the motor densities given in Eqs. (4) and (5) to represent the aster. We then evolve these equations in time until the steady state is reached. We compare the motor profiles obtained in such simulations to profiles obtained from solving the ordinary differential equation at steady state [Eq. (26)] by a fourth order Runge-Kutta method. Free and bound motor densities at the boundary of the system are obtained by solving the full time-dependent equations [Eqs. (4) and (5)]. These are used as boundary value input to the Runge-Kutta procedure to facilitate direct comparison between simulation and analytic results.

Using the symmetry of the scaled equations Eqs. (4) and (5) discussed in Sec. II, we normalize the densities obtained by these two methods to the same constant value before comparing them. Figure 7 shows a plot of the distribution of bound motors in a single aster obtained from (i) the direct simulation, (ii) the Runge-Kutta method, and (iii) the exact solution outlined in the previous section. The parameter values are $\gamma_{f\to b}=\gamma_{b\to f}=0.5$ and $m=0.5$. Figure 8 shows the comparison between simulations, the Runge-Kutta method, and the exact solution for the free motor density profiles. While the data are noisy, particularly for the bound motor densities, the agreement with the theoretically predicted result is satisfying.

Figure 9 shows the distribution of bound motors in a vortex configuration obtained by fixing $\mathbf{T}=\hat{\boldsymbol{\theta}}$ in the full equations of motion for the motor densities given in Eqs. (4) and (5). The plot of $m_b(r)$ vs r illustrates the slow, essentially logarithmic variation of the motor densities in such configurations, consistent with the analytic approach of this paper and of earlier work.

D. Saturation effects and the stabilization of asters

So far, in our analysis, we have ignored the effects of interactions between bound motors. These motors, in their

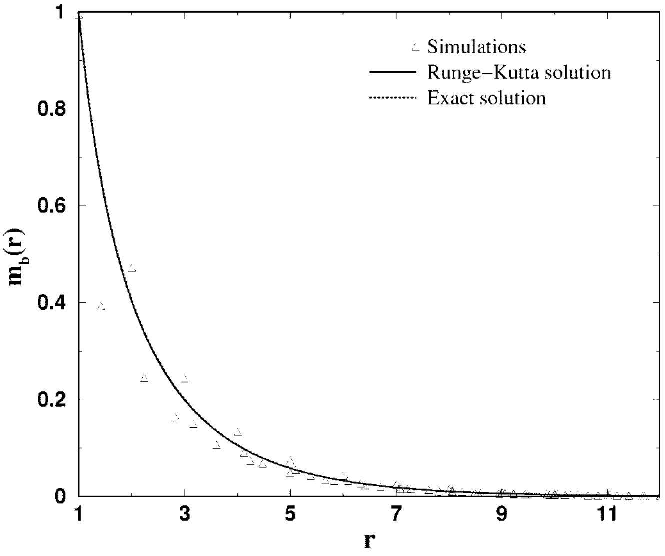

FIG. 7. Density profiles for bound motor densities (plotted in dimensionless units). The profiles are shown for an aster in the regime $\gamma_{f\to b}=\gamma_{b\to f}=0.5$, with $S=0$. The density is chosen to be 0.5. The *x* axis denotes the separation from the center of the aster in units of the lattice spacing.

physical setting, have a finite size and move on a one-dimensional track, the microtubule. It is thus reasonable to expect that interactions between bound motors should become increasingly important at large motor densities. One can account for these interactions by simply requiring that more than one motor cannot occupy the same volume in space at the same time. Such "excluded volume" interactions have been used in earlier models for collective effects in molecular motor transport [27].

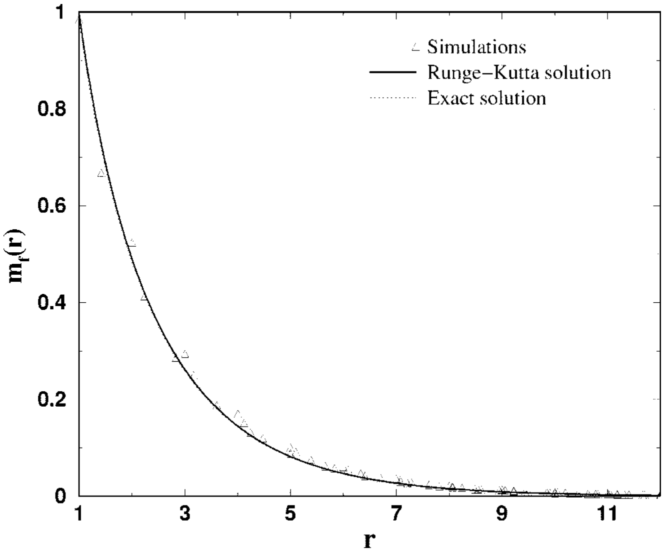

FIG. 8. Density profiles for free motor densities plotted in dimensionless units. The profiles are shown for an aster in the regime $\gamma_{f\to b}=\gamma_{b\to f}=0.5$ and $S=0$. The density is chosen to be 0.5. The *x* axis denotes the separation from the center of the aster in units of the lattice spacing.

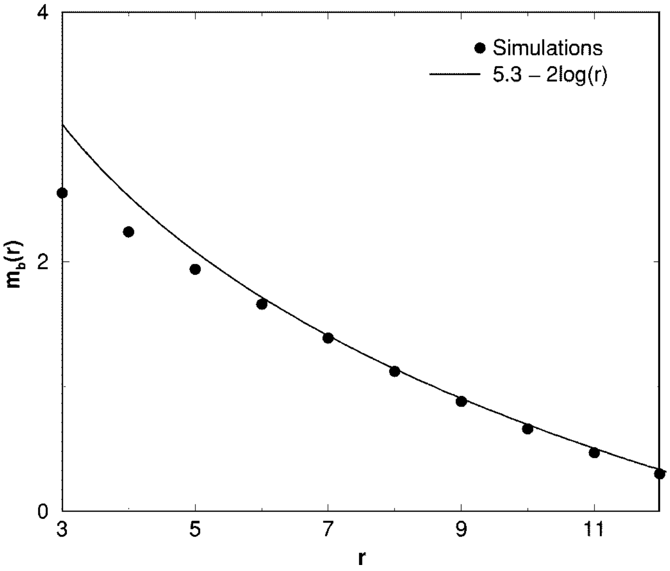

FIG. 9. Density profiles for bound motor densities plotted in dimensionless units. The profiles are shown for a vortex in the regime $\gamma_{f\to b}=\gamma_{b\to f}=0.5$ and $S=0$. The density is chosen to be 0.5. The *x* axis denotes the separation from the center of the vortex in units of the lattice spacing.

At the simplest level, accounting for such interactions leads to a nonlinear (in general, also nonmonotonic) dependence of the motor current on the density. This can be incorporated in our calculation by choosing a motor current of the form

$$\mathbf{J}_{m_b} = A m_b\, f(m_b)\mathbf{T}. \tag{37}$$

The function $f(m_b)$ should, in principle, be calculated from an underlying microscopic model. We will circumvent this necessity by simply assuming a convenient form purely for illustrative purposes which is (a) consistent with the requirement that A (the velocity) is density independent for small m_b densities and (b) saturates for large m_b. One such choice is

$$f(m_b) = 1 - \tanh(m_b/m_{sat}). \tag{38}$$

The value m_{sat} limits the current of bound motors. When $m_{sat} \gg m_b$ then $f(m_b)\to 1$ and we recover results discussed earlier. When $m_{sat} \ll m_b$, the current reduces as $f(m_b)\to 0$. In the aster case ($\mathbf{T}=-\hat{\boldsymbol{r}}$), Eq. (25) becomes

$$\partial_r\, m_f(r) = -\, m_b(r) f(m_b). \tag{39}$$

Therefore, the free motors obey

$$\partial_r^2 m_f + \left(\frac{1}{r} - \gamma_{b\to f}/f(m_b)\right)\partial_r m_f - \gamma_{f\to b} m_f = 0. \tag{40}$$

This equation can now be solved as a boundary value problem using the methods described earlier.

Figure 10 shows bound motor densities $m_b(r)$ as a function of r for different values of m_{sat}. We have normalized each of the plots to the same value at the origin. We choose $m_{sat}=0.001$, 0.1, 1, and 1000. An increased m_{sat} implies smaller saturation effects. The plots shown in Fig. 10 are normalized to unity at $r=1$. Observe that reducing m_{sat} leads to far smoother variations of the bound motor density. Data

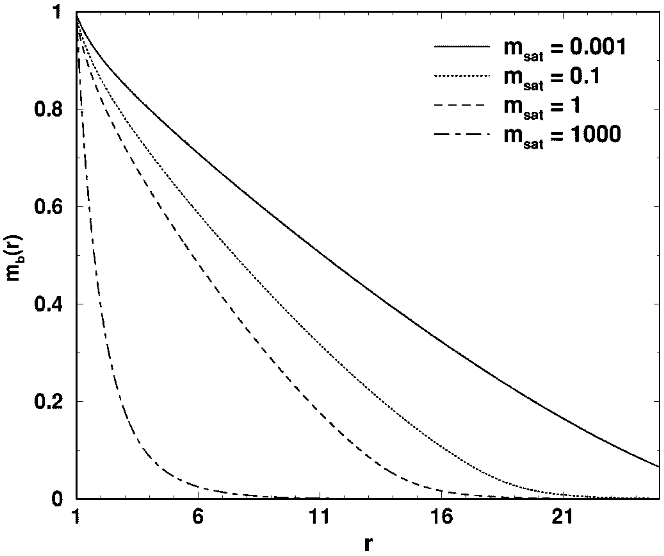

FIG. 10. Effect of saturation on the motor density profile in asters. As the effect of saturation is increased, the profile is smoother. The curves are labeled from left to right as m_{sat}=1000,1.0,0.1,0.0001. The x axis denotes the separation from the center of the aster in units of the lattice spacing; the y axis is plotted in dimensionless units.

for the associated free motor densities are similar and are not shown here.

It is tempting to directly link such saturation effects with the experimental observation of bundles of microtubules at large motor densities. Physically, while alignment would be favored at large motor densities, saturation should set limits on such alignment, perhaps favoring instead the locally aligned "bundles" seen at large m. Unfortunately, we have been unable to stabilize solutions of the full set of equations governing pattern formation incorporating saturation effects and so are unable to test this interesting possibility directly.

V. RELATIVE STABILITY OF ASTERS AND VORTICES

Lee and Kardar rationalize the stability of vortices (at $S=0$) compared to asters in the following way. If $\epsilon=1$, the right-hand-side of the tubule equation derived by LK can be interpreted as the functional derivative of a "free energy." The motor density profile plays the role of a spatially modulated stiffness. This enables the calculation of the relative "free energies" of aster and vortex states. Smoother motor density profiles lead to lower "free energies." The reduced energy of the vortex configuration, in which motor density profiles decay logarithmically, implies its increased stability as compared to asters, for which motor density profiles decay exponentially away from the core.

We adapt the Lee-Kardar argument to our model, using our analytic results for bound motor density profiles in asters and vortices. In Fig. 11, we show the *modulus* of the difference in energy of a single vortex and a single aster as a function of the system size for our model and for the Lee-Kardar model. We work at the same value of total motor density m in each case, setting $\epsilon=1$. Since the magnitude of "energy" scales in the two models differs, the behavior of the energy difference is most clearly seen using a logarithmic scale for the y axis. The point at which the vortex energy is reduced below the aster energy appears as the minimum in the curve. From the position of this minimum, we see that the crossover length scale above which asters are unstable with respect to vortices is smaller in the Lee-Kardar model as compared to our model.

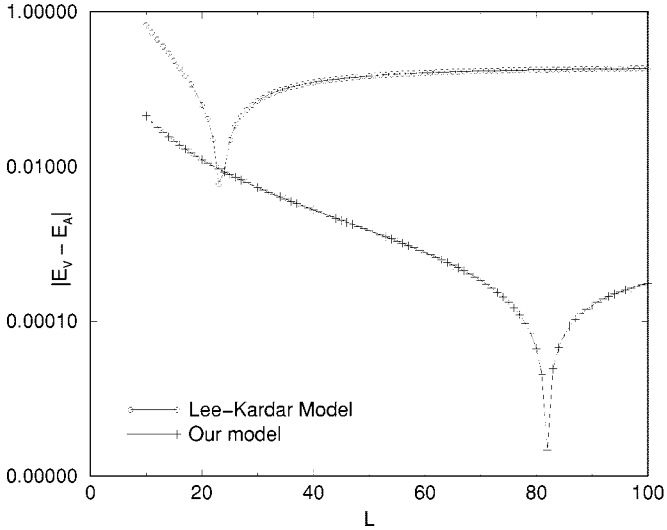

FIG. 11. A plot of the difference in energies (in dimensionless form) of a single vortex and a single aster versus the system size L. The parameter values are $m=1$, $\epsilon=1$, and $S=0$. The y axis (system size in dimensionless units) is plotted on a logarithmic scale. The point at which the energy of the vortex becomes lower than the energy of the aster shows up as the minimum in this curve. In the Lee-Kardar model the length scale at which the vortex becomes lower in energy is about four times smaller than in our model, for this choice of parameter values.

The fact that this crossover length scale lies between 50 and 100 in our units for length rationalizes our observation that the stable asters we obtain for $L=50$ are replaced by stable vortices for $L=100$. These results support, and add further credence to, the Lee-Kardar argument, at least in the $S=0$ case. With finite S, of course, vortices are disfavored altogether and generating stable aster structures is no longer an issue.

We now provide a qualitative explanation of three basic features of motor and microtubule arrangements at zero and nonzero S. These are (i) the absence of vortices at nonzero S, (ii) the presence of a small number of large asters at small S, vs (iii) the presence of a large number of small asters which increases as S for larger S. Our approach is approximate and qualitative, based on "free energy" type arguments, analogous to those of Lee and Kardar.

Consider the limit in which $\epsilon=1$ and the ∇m term is obtained through a functional differentiation of the "free-energy" term

$$E_S = \int d^2x \left(\alpha \nabla \cdot \mathbf{T} + \frac{S}{\alpha} m_b \right)^2 . \tag{41}$$

A functional derivative of F with respect to the $\mathbf{T}$ field generates the terms $\alpha^2 \nabla(\nabla \cdot \mathbf{T})$ and $S \nabla m_b$. In the limit that $\alpha \to 0$, we obtain the ∇m_b term of our equation of motion. (We prefer to work with a nonvanishing, although infinitesimal, value of α and to consider the effects of varying S, to avoid the singular behavior that arises in the $\alpha = 0$ limit.) Our introduction of the term in S was, in fact, motivated by the observation that motors moving along two initially parallel microtubule configurations, act to bring them together, favoring a nonzero divergence. This physics, although incorporated in the simulations of Nédéléc *et al.*, is ignored in the LK model.

The full "free energy" for the $\mathbf{T}$ field is

$$E = \int d^2x \left[-\frac{1}{2}\alpha |T|^2 + \frac{1}{4}\beta |T|^4 + \frac{1}{2} m_b(r)(\nabla \mathbf{T})^2 + \frac{1}{2}\left(\alpha \nabla \cdot \mathbf{T} + \frac{S}{\alpha} m_b \right)^2 \right]. \tag{42}$$

We fix the modulus of $\mathbf{T}$, thereby eliminating the first two terms, and concentrate on the relative energetics of states governed by the last two terms of the equation.

For the Lee-Kardar model, with $S = 0$, the stability of vortices over asters can be understood from simple comparisons of the relative energies of vortices and asters. First consider the case of a single aster. We choose a simplified profile for bound motors, assuming

$$m_b = \begin{cases} A, & r \leq \xi, \\ 0, & r > \xi. \end{cases} \tag{43}$$

This represents, although approximately, the fact that microtubule densities are significant only over distances of order ξ from the core of the aster. The factor A is a normalization factor which ensures a fixed number of motors N in a system of typical size L. We will work with a fixed overall density of motors $\sim N/L^2$ and examine the limit in which $L \to \infty$.

In the $S = 0$ limit, the energy E_A of the aster is dictated by

$$E_A^0 \sim \int_a^L d^2r \, m_b(r)(\nabla \mathbf{T})^2 \sim A \ln(\xi/a), \tag{44}$$

where we cut the integral off at a lower limit a corresponding to a microscopic coarse-graining scale and have used the fact that $(\nabla \mathbf{T})^2 = 1/r^2$ for both asters and vortices. We now fix A by normalization: since $\int_a^L m(r) d^2r = N = nL^2 \sim A\xi^2$, we obtain $E_A^0 \sim nL^2 \ln(\xi/a)/\xi^2$. (Accounting for a more complex decay of the bound motor density does not change this result qualitatively.) Thus, for a system of size L $(L \gg \xi)$, imposing a fixed *density* of motor yields a quadratic increase of the energy with system size L.

We now repeat the same argument with a single vortex. Here, the relatively slower variation $m_b(r) \sim C_1 + C_2 \ln(r/\lambda)$ yields $E_v^0 \sim \int_a^L [m_b(r)/r^2] r \, dr \sim \ln(L/a)$, up to further logarithmic corrections. The prefactor is then *independent* of system size, leading to an overall logarithmic increase of energy with system size, a far weaker function than the quadratic dependence on L of the aster. This implies that for sufficiently large L the energy of the isolated vortex falls below that of a single aster, in systems of sufficiently large sizes, as first suggested by Lee and Kardar.

How are these arguments modified at finite S? Since simulations indicate that the state obtained at finite positive S is a "lattice of asters" with the scale of the aster decreasing as S is increased, we will compare the energies of single vortex configurations with energies for an assembly of asters ("miniasters") of typical size σ. We imagine that the $L \times L$ system is subdivided into $\sigma \times \sigma$ units and place an aster in each one of these subunits. For a system of linear size L, the number density of such asters is ϕ. For inward pointing asters, as obtained in our calculation, the divergence $\nabla \cdot \mathbf{T} = -1/r$. Consider first the term

$$E_S \sim \int d^2x \left[\alpha \nabla \cdot \mathbf{T} + \frac{S}{\alpha} m_b(r) \right]^2 . \tag{45}$$

Now miniasters (i) are assumed small and (ii) obey boundary conditions that differ from the case of the single system-size spanning aster. Bound motor profiles are then, in general, combinations of the two solutions obtained earlier rather than the single one which yielded the exponentially damped form used in our earlier analysis. Also, the close proximity of the many miniasters formed indicates a slower than exponential variation of the bound motor densities about each one. Let us *assume* that motor densities in such miniasters adjust in order that the following motor density profile is obtained: $m_b(r) \sim \alpha^2/Sr (r \leq \sigma)$ and $m_b(r) \sim 0 (r > \sigma)$. This ensures that the contribution of the term above is canceled. Note that the bulk of the contribution to the energy of a miniaster comes from the region $r \leq \xi$; the contributions from larger regions is negligible provided $\xi \sim \sigma$.

We first calculate the energy E_{1mA} of a single such miniaster configuration. This is obtained from the integral

$$E_{1mA} = \int_a^L d^2r m_b(r)(\nabla \mathbf{T})^2 \sim \frac{\alpha^2}{S} \int_a^\sigma dr \frac{1}{r^2} \sim \frac{\alpha^2}{Sa}. \tag{46}$$

The number of motors in a single miniaster is obtained from

$$N_{1mA} \sim \int_a^\sigma m(r) d^2r \sim \frac{\alpha^2 \sigma}{S}. \tag{47}$$

The total energy E_{mA}^T of the system of miniasters is then

$$E_{mA}^T \sim \frac{\alpha^2}{Sa} \phi L^2 . \tag{48}$$

The constraint $n = \phi N_{1mA}$ yields

$$\phi \sim \frac{S}{\alpha^2 \sigma}, \tag{49}$$

illustrating how the number of asters increases as S is increased. The total energy corresponding to a fixed areal density of motors n is then easily derived as

$$E_{mA}^T \sim \frac{nL^2}{\sigma a}. \tag{50}$$

We now compare this with the energy of a single vortex at nonzero S, computed assuming that the motor density profiles are the same as in the case in which S was zero. This is obtained as $E_v \sim S^2 n^2 L^2 / \alpha^2$, yielding the ratio

$$\frac{E_V}{E_{mA}^T} \sim \frac{nS^2 \sigma a}{\alpha^2}. \tag{51}$$

We may also compare the energy of an assembly of miniasters with the energy of a single aster. Arguments similar to those above yield $E_A \sim n^2 S^2 L^2 / \alpha^2$, and thus

$$\frac{E_A}{E_{mA}^T} \sim \frac{nS^2 \sigma a}{\alpha^2}. \tag{52}$$

Note that both these arguments indicate that as α is reduced towards zero (or S is increased from a nonzero value), both single asters and single vortices are unstable to an array of miniasters. At infinitesimal α, provided S is nonzero, our results indicate that the number density of miniasters increases with S (linearly in the simple argument given here), with the size of each aster decreasing in proportion. The arguments given here rest on the assumption that the motor distribution in asters adjusts so as to minimize the cost for the term involving S. No such adjustment can lower the energy of single vortex configurations.

VI. CONCLUSIONS

This paper presents a hydrodynamic theory of pattern formation in motor-microtubule mixtures, studying both the effects of confinement as well as pattern formation in unconfined geometries. We show that the influence of the boundaries on pattern formation can be considerable, by illustrating how either asters or vortices can be formed depending on how the orientation of microtubules is fixed at the boundary. We have explored the parameter space of ϵ, m, and S systematically, describing the variety of configurations obtained. We obtain density distributions of free and bound motors corresponding to the final microtubule configurations. Such plots may be compared directly to experiments. We have compared analytic predictions for motor density profiles in isolated vortices and asters with simulation data. We have also presented results for pattern formation in much larger systems, in which the effects of boundaries were minimal.

One technical improvement would be to account for variations in the local *density* of microtubule, as opposed to only their orientation. We could then account for the density dependence of quantities such as $\gamma_{f\to b}$. More information from experiments, performed in confined geometries using motors with a range of different processivities would also be useful in clarifying some of the issues which relate to the simulations described here. It would also be interesting to search for the novel configurations we obtain here in different regimes of parameter space, such as the "flag," the distorted vortex and the "outward aster."

As we have emphasized, the set of hydrodynamic equations we motivate and use allow for a minimal yet complete description of the patterns formed in mixtures of motors and microtubules. We have suggested elsewhere [12] that it may be useful to think of spindle formation itself as a pattern formation problem which can be modeled using continuum hydrodynamical equations in a small number of variables. One intriguing possibility is that the bipolar aster conformation of microtubules seen in the spindle is associated with parameters in our model in which the formation of a small number of large asters is favored. It is tempting to think of changes in the structure of the spindle as mitosis proceeds as reflecting the dynamics of an underlying few parameters in simplified models such as this. Further work relating to this program is in progress.

ACKNOWLEDGMENTS

We thank Y. Hatwalne, Madan Rao, Sitabhra Sinha, and G. Date for useful and illuminating discussions. P.B.S thanks IBM for providing computational facilities under a shared university research grant.

APPENDIX: NUMERICAL METHODS

We solve Eqs. (4)–(6) numerically on an $L \times L$ square grid indexed by (i,j) with $i=1,\ldots,L$ and $j=1,\ldots,L$ [24]. The equation for the free motor density is evolved through a Euler scheme,

$$m_f(t+\Delta t) = m_f(t) - \Delta t \, \nabla \cdot J(m_f) - \gamma_{f\to b} m_f + \gamma_{b\to f} m_b, \tag{A1}$$

where

$$J_x(m_f(i,j)) = [m_f(i+1,j) - m_f(i-1,j)]/2\delta, \tag{A2}$$

$$J_y(m_f(i,j)) = [m_f(i,j+1) - m_f(i,j-1)]/2\delta. \tag{A3}$$

The grid spacing is $\delta x = \delta y = \delta = 1$ and the time step $\Delta t = 0.1$. At the boundaries, we impose the boundary condition that no current (either of free or bound motors) flows into or out of the system. This condition is easily imposed by setting the appropriate current to zero.

A related discretization is used for the bound motor density equation

$$\partial_t m_b = - \nabla \cdot (m_b \mathbf{T}) + \gamma_{f\to b} m_f - \gamma_{b\to f} m_b, \tag{A4}$$

where, in the bulk, partial derivative terms are discretized as

$$\partial_x(m_b \mathbf{T}) = [m_b(i+1,j)T_x(i+1,j) - m_b(i-1,j)T_x(i-1,j)]/2\delta \tag{A5}$$

with a similar equation used for the y component.

The $\mathbf{T}$ equation is differenced through the alternate direction implicit operator splitting method in the Crank-Nicholson scheme. At the first half time step

$$(r\mathcal{I} - \mathcal{L}_x) T_x^{n+1/2} = (r\mathcal{I} + \mathcal{L}_y) T_x^{n}, \tag{A6}$$

where $r = 2\delta^2/\delta t$ and $\mathcal{I}$ is the identity matrix. The superscripts on T_x indicate the time step at which these quantities are calculated. The operators $\mathcal{L}_x$ and $\mathcal{L}_y$ are given by

$$\mathcal{L}_x = m_b \partial_x^2 + (\partial_x m_b)\partial_x + S(\partial_x m_b), \tag{A7}$$

$$L_y = 2C(1 - T^{2}) + m_b \partial_y^{2} + (\partial_y m_b)\partial_y + S(\partial_y m_b). \quad \text{(A8)}$$

The first and second derivatives evaluated for a function $f(i,j)$ on a lattice point (i,j) in the bulk are

$$\partial_x f(i,j) = [f(i+1,j) - f(i-1),j)/2\delta, \quad \text{(A9)}$$

$$\partial_x^{2} f(i,j) = [f(i+1,j) - 2f(i,j) + f(i-1,j)]/\delta^{2}, \quad \text{(A10)}$$

with similar equations for the y derivatives.

At the second half time step,

$$(r\mathcal{I} - \mathcal{L}_y)T_x^{n+1} = (r\mathcal{I} + \mathcal{L}_x)T_x^{n+1/2}, \quad \text{(A11)}$$

where

$$\mathcal{L}_x = m_b \partial_x^{2} + (\partial_x m_b)\partial_x + S(\partial_x m_b), \quad \text{(A12)}$$

$$\mathcal{L}_y = m_b \partial_y^{2} + (\partial_y m_b)\partial_y + S(\partial_y m_b). \quad \text{(A13)}$$

A similar scheme is used for differencing the equation for the T_y component. Our simulations are on lattices of several sizes, ranging from $L=30$ to $L=200$. We vary the motor density in the range 0.01 to 5 in appropriate dimensionless units. We work with two different types of boundary conditions on the T field. In the first, which we refer to as reflecting boundary conditions, the microtubule configuration at the boundary sites is fixed to point along the inward normal. In the second, which we refer to as parallel boundary conditions, microtubule orientations at the boundary are taken to be tangential to the boundary. In both these sets of boundary conditions, the state of the boundary T vectors is fixed and does not evolve. The total number of motors, initially divided equally between free and bound states and distributed randomly among the sites, is explicitly conserved.

We add weak noise, primarily in the $\mathbf{T}$ equation of motion, to ensure that true steady states are reached in our simulations. This noise is drawn from a Gaussian distribution with zero mean, δ-function correlated in time, and thus with a strength specified solely by its variance. Such noise simulates thermal and nonequilibrium fluctuations, such as arise from the stochastic process of ATP hydrolysis by motors. Large noise strengths wipe out patterns, yielding homogeneous states. We have also experimented with a variety of initial states to ensure that the qualitative features of the patterns we obtain as stable steady states are, indeed, robust.

---

[1] B. Alberts, A. Johnson, J. Lewis, M. Raff, K. Roberts, and P. Walter, *Molecular Biology of the Cell*, 4th ed. (Garland Science, New York, 2002).

[2] Microtubules *in vitro* undergo an alternating process of rapid, stochastic polymerization and depolymerization (dynamic instability) unless stabilized.

[3] S. A. Endow and D. S. Barker, Annu. Rev. Physiol. **65**, 161 (2003).

[4] V. Rodionov and G. Borisy, Nature (London) **386**, 170 (1997).

[5] F. Nédélec, T. Surrey, A. C. Maggs, and S. Leibler, Nature (London) **389**, 305 (1997).

[6] R. Heald, R. Tournebize, A. Habermann, E. Karsenti, and T. Hyman, J. Cell Biol. **138**, 615 (1997); R. Heald, R. Tournebize, T. Blank, R. Sandaltzopoulos, A. Hyman, and E. Karsenti, Nature (London) **382**, 420 (1996).

[7] L. Hartwell, J. Hopfield, S. Leibler, and A. Murray, Nature (London) **402**, C 47 (1999).

[8] T. Surrey, F. Nédélec, S. Leibler, and E. Karsenti, Science **292**, 1167 (2001).

[9] F. Nédélec and T. Surrey, C. R. Acad. Sci., Ser IV: Phys., Astrophys. **2**, 841 (2001).

[10] F. Nédélec, J. Cell Biol. **158**, 1005 (2002).

[11] F. Nédélec, T. Surrey, and E. Karsenti, Curr. Opin. Cell Biol. **23**, 118 (2003).

[12] S. Sankararaman, G. I. Menon, and P. B. Sunil Kumar, Phys. Scr., T **106**, 26 (2003).

[13] Since the experiments are performed in a confined geometry, the otherwise long-ranged hydrodynamic interaction is screened because the boundaries of the system act as a sink for momentum. Neglecting the role played by hydrodynamics is therefore justified.

[14] H. Y. Lee and M. Kardar, Phys. Rev. E **64**, 056113 (2001).

[15] F. Nèdèlec, T. Surrey, and A. Maggs, Phys. Rev. Lett. **86**, 3192 (2001).

[16] J. Kim, Y. Park, B. Kahng, and H. Y. Lee, J. Korean Phys. Soc. **42**, 162 (2003).

[17] Lee *et al.* [16] generalize the LK model to account for both bound and free motors and allow the rate at which motors hop on to the microtubule to depend on the local microtubule density. They obtain steady state patterns consistent with the LK model—a single vortex at large motor densities—and predict a logarithmic decay of the free motor density around a vortex. The nature of the states obtained in this calculation is very similar to the ones obtained by Lee and Kardar. Our critique of the Lee-Kardar model above applies to these results as well.

[18] K. Kruse and F. Julicher, Phys. Rev. Lett. **85**, 1778 (2000); Phys. Rev. E **67**, 051913 (2003); K. Kruse, S. Camalet, and F. Julicher, Phys. Rev. Lett. **87**, 138101 (2001).

[19] J. Toner and Y. Tu, Phys. Rev. E **58**, 4828 (1998); Phys. Rev. Lett. **75**, 4326 (1995).

[20] T. B. Liverpool and M. C. Marchetti, Phys. Rev. Lett. **90**, 138102 (2003).

[21] T. B. Liverpool and M. C. Marchetti, e-print cond-mat/0406276.

[22] We only fail to obtain “bundles,” a disordered phase obtained at still higher densities of motors.

[23] We find it convenient to refer to the distinct states seen in the experiments and our simulations as “phases,” insofar as quantitative distinctions can be made between them and they are well contrasted from the point of view of the experiments. However, such terminology is, strictly speaking, inaccurate since we believe that sharp qualitative distinctions between several of these states, such as the disordered phase, the aster-vortex mixture, and the lattice of vortices cannot be made—a

more generic name would be a disordered and/or aster-vortex mixture dominated by arrested states at low motor density [14] in this regime.

[24] W. Press, S. Teukolsky, W. Vetterling, and B. Flannery, *Numerical Recipes in C* (Cambridge University Press, Cambridge, U.K., 1998).

[25] We have also performed a linear stability analysis of the equations governing our model starting from the uniform state ($|\hat{\mathbf{T}}|=1$, all $\mathbf{T}$ aligned), with the motor densities constant, consistent with periodic boundary conditions on the fields. We choose $m_f^0=C_1$ and $m_b^0=C_2$ where C_1 and C_2 satisfy $\gamma_{f\rightarrow b}C_2=\gamma_{b\rightarrow f}C_1$. Straightforward analysis yields the following results. The uniform state favored by periodic boundary conditions is stable over the range of parameters we use, *provided* $S=0$. At any nonzero S, the solutions are linearly unstable over the full range of parameters. We note that this particular solution, with its associated boundary condition, corresponds to a macroscopic flux of motors entering and leaving the system through its boundaries. This is physically unrealistic, given the experimental system.

[26] We remind the reader that single system-spanning vortices and asters are obtained strictly in the $S=0$ limit of Eqs. (4)–(6). For nonzero S, the steady state configuration is a lattice of asters.

[27] Y. Aghababaie, G. I. Menon, and M. Plischke, Phys. Rev. E **59**, 2578 (1999).